JOURNAL OF SPACECRAFT AND ROCKETS
Vol. 46, No. 3, May–June 2009

Numerical Study of Plasma-Assisted Aerodynamic Control for Hypersonic Vehicles

Nicholas J. Bisek* and Iain D. Boyd†
University of Michigan, Ann Arbor, Michigan 48109
and
Jonathan Poggie‡
U.S. Air Force Research Laboratory, Wright–Patterson Air Force Base, Ohio, 45433-7512

DOI: 10.2514/1.39032

Plasma actuators and various forms of volumetric energy deposition have received a good deal of research attention recently as a means of hypersonic flight control. An open question remains as to whether the required power expenditures for such devices can be achieved for practical systems. To address this issue, a numerical study is carried out for hypersonic flow over a blunt-nose elliptic cone to determine the amount of energy deposition necessary for flight control. Energy deposition is simulated by means of a phenomenological dissipative heating model. A parametric study of the effects of energy deposition is carried out for several blunt elliptic cone configurations. Three different volumetric energy deposition patterns are considered: a spherical pattern, a "pancake" pattern (oblate spheroid), and a "bean" pattern (prolate spheroid). The effectiveness of volumetric energy deposition for flight control appears to scale strongly with a nondimensional parameter based on the freestream flow kinetic energy flux.

Nomenclature

A	=	surface area of grid cell
a, b, c	=	the equatorial radii and the polar radius of an ellipsoid
C_m	=	moment coefficient, $[2M_p]/[\rho_\infty u_\infty^2 L^2 d]$
C_p	=	pressure coefficient, $[2(p_w - p_\infty)]/[\rho_\infty u_\infty^2]$
d	=	maximum spanwise length
E	=	total energy per volume
h	=	enthalpy
i, j, k	=	computational grid indices along the axial, radial, and circumferential directions
$\mathbf{J}$	=	mass diffusion flux, x, y, z directions
L	=	axial surface length
M_p	=	moment about center of gravity
$\mathbf{n}$	=	normal vector
p	=	pressure
Q	=	total power input by actuator
$\mathbf{q}$	=	heat flux, translational–rotational and vibrational–electronic
$\tilde{Q}$	=	nondimensional total power input by actuator, $Q/(\rho_\infty u_\infty^3 L^2)$
Re_x	=	running Reynolds number, $\rho_\infty u_\infty x/\mu_\infty$
S	=	source term
St	=	Stanton number, $q_w/[\rho_\infty u_\infty (h_0 - h_w)]$
T	=	temperature, translational and rotational
T_v	=	temperature, vibrational and electronic
$\mathbf{u}$	=	velocity vector (u, v, w)
x, y, z	=	streamwise, spanwise, and transverse coordinates
ϵ	=	emissivity
θ	=	angle along circumference of the body, cylindrical coordinate system
λ	=	characteristic length
μ	=	coefficient of viscosity
ρ	=	mass density
σ	=	Stefan–Boltzmann constant, 5.67×10^{-8} W/[m^2 K^4]
τ	=	viscous stress
ϕ	=	inclination of the deposition to the freestream flow

Subscripts

s	=	species
w	=	wall
0	=	stagnation
∞	=	freestream

Presented as Paper 4226 at the 39th Plasmadynamics and Lasers Conference, Seattle, WA, 23–26 June 2008; received 11 June 2008; accepted for publication 26 January 2009.

*Graduate Student, Department of Aerospace Engineering, 1320 Beal Avenue. Student Member AIAA.
†Professor, Department of Aerospace Engineering, 1320 Beal Avenue. Associate Fellow AIAA.
‡Senior Aerospace Engineer, AFRL/RBAC, 2210 Eighth Street, Building 146, Room 225. Associate Fellow AIAA.

I. Introduction

AERODYNAMIC control and drag reduction are major challenges for hypersonic vehicle designers. A good deal of research attention has recently focused on hypersonic plasma interactions and plasma flow control to explore ways of confronting these challenges [1,2].

Minimizing drag in vehicle design leads to long, thin bodies with sharp leading edges. This constrains the materials available for the vehicle's thermal protection system (TPS) because there is a required minimum thickness that may not be achieved for a given vehicle configuration. In addition, small defects in the production of the sharp edges can result in serious or even catastrophic problems for the TPS [3]. Blunting the leading edge reduces these drawbacks but results in a much larger wave drag [4]. Recent experimental and computational research by Shang et al. [5] has investigated ways of reducing drag on blunt-nose bodies by means of plasma injection, and research by Kremeyer et al. [6] and Yan and Gaitonde [7] focused on drag reduction and flow control using laser deposition (filamentation) ahead of conic and spherical geometries. Riggins and Nelson [8] used volumetric heating in front of the bow shock to reduce drag for 2-D hypersonic blunt bodies. Virtual cowls for off-design scram engines have also been studied using electron beam ionization by Macheret et al. [9] and dc discharges by Shang et al. [10].

In addition to these design constraints, traditional control surfaces (flaps) need to be positioned away from the center of gravity to extend the maneuverability of the vehicle. The location of such flaps

is limited because the bow shock surrounding the vehicle will impinge on surfaces that extend beyond the shock envelope. This results in extreme pressure and heat transfer rates at the impingement point. As such, vehicle configurations tend to be streamlined with minimal protrusions from the fuselage. Mechanically driven flaps require clearance below the surface of the flap to provide space for the flap control arm and a strong attachment point to push from. In addition, there is a small gap in the TPS as the flap extends out to deflect the flow. This gap is difficult to protect and can cause heat-related damage to the vehicle. In addition, sustained cruise and other long-duration hypersonic missions also suffer from nonuniform ablation of the flap causing nonuniform control authority on the vehicle.

Plasma actuators are advantageous over mechanical controllers because they do not have moving parts, can be located either in or beneath the TPS, and are uninhibited by the bow shock. This extends the range of possible locations for the actuator and allows for multiple actuators to be powered by a central energy source. They can potentially be turned on and off very rapidly and should have a minimal aerothermal penalty when turned off. Plasma actuators can serve multiple roles. They can be used to provide steering moments [11,12], changes in vehicle lift [13], control of flow separation [14,15], and local heat load mitigation [16].

The primary objective of this research effort is to determine whether a useful degree of flight control can be achieved with practical levels of energy deposition by investigating the effects of energy deposition on a realistic hypersonic vehicle and its surrounding flowfield. In the following, we first present validation studies of the flow code LeMANS (Michigan aerothermodynamic Navier–Stokes) using relevant experimental data available in the literature. Having successfully validated LeMANS, the code is applied to investigate plasma-based aerodynamic control. We investigate how the shape, location, and input power of deposition affect vehicle control. In addition, hot wall effects, thermodynamic models, and additional vehicle configurations are explored to help draw conclusions over different flight regimes.

II. Method

Flowfield results are obtained using computational fluid dynamics (CFD) to solve the Navier–Stokes equations. The CFD computations are executed using the LeMANS code, which was developed at the University of Michigan [17–20].

LeMANS is a general 2-D/axisymmetric/3-D, parallel, unstructured, finite-volume CFD code. The numerical fluxes between cells are discretized using a modified Steger–Warming flux vector splitting (FVS) scheme, except near shock waves. In these regions the original Steger–Warming FVS scheme is used.

LeMANS may be employed with any of three thermodynamic models: perfect gas, equilibrium thermochemistry, and nonequilibrium. LeMANS employs a two-temperature model to account for thermal nonequilibrium and a standard finite-rate chemistry model for nonequilibrium chemistry. The two-temperature model assumes that a single temperature T accounts for the translational and rotational energy modes of all species whereas the vibrational and electronic energy modes are accounted for by a separate temperature T_v.

The simulations are performed using second-order accurate spatial discretization and carry double-precision arithmetic throughout. Thermal equilibrium and a 5-species finite-rate air chemistry model (N_2, O_2, NO, N, and O) are used in the simulations presented unless otherwise stated.

For a single temperature (equilibrium) model with finite-rate chemistry

$$\frac{\partial \rho_s}{\partial t} + \nabla \cdot (\rho_s \mathbf{u} + \mathbf{J}_s) = \dot{\omega}_s \tag{1}$$

$$\frac{\partial \rho \mathbf{u}}{\partial t} + \nabla \cdot (\rho \mathbf{u}^2 + p\delta - \tau) = 0 \tag{2}$$

$$\frac{\partial E}{\partial t} + \nabla \cdot ((E + p)\mathbf{u} - \tau \cdot \mathbf{u} - \mathbf{q} + \Sigma \mathbf{J}_s h_s) = S \tag{3}$$

For the two-temperature (nonequilibrium) cases, the following vibrational energy equation is also employed:

$$\frac{\partial E_v}{\partial t} + \nabla \cdot ((E_v)\mathbf{u} - q_v + \Sigma \mathbf{J}_s e_{v,s}) = \dot{\omega}_v \tag{4}$$

LeMANS assumes the fluid is continuous and Newtonian. It assumes Stokes' hypothesis when determining the viscous stresses. The species mass diffusion flux ($\mathbf{J}_s$) is determined using Fick's law modified to enforce that the sum of the diffusion fluxes is zero and plasma charge neutrality. A harmonic oscillator is used to model the species vibrational energy per unit mass ($e_{v,s}$).

For the nonequilibrium cases, we assume that 100% of the deposition energy goes initially into the translational energy equation. As the solution converges, some of the energy transfers into the vibrational energy equation by means of the source term ($\dot{\omega}_v$). Production of vibrational energy ($\dot{\omega}_v$) is due to reactions in the finite-rate chemistry model and energy exchange between the translational–rotational and the vibrational–electronic energy modes. Deposition of all the energy into the translational mode is a strong assumption but is adequate for the purpose of illustrating the effects of thermal nonequilibrium.

A thermal actuator is considered as the plasma control device in this study. It is represented by a phenomenological model of dissipative heating. This model is accounted for in the Navier–Stokes equations by the addition of a source term S to the right side of energy Eq. (3). The shape and location of the actuator are modeled with contours of constant S having an ellipsoidal shape [21]. The strength or total power deposited into the flow uses exponential decay from the centroid of the energy deposition pattern

$$S = \frac{Q}{\pi^{3/2} a \cdot b \cdot c} e^{(-(\frac{\hat{x}}{a})^2 - (\frac{\hat{y}}{b})^2 - (\frac{\hat{z}}{c})^2)} \tag{5}$$

$$\begin{aligned} \hat{x} &= (x - x_0)\cos\phi - (z - z_0)\sin\phi \qquad \hat{y} = (y - y_0) \\ \hat{z} &= (x - x_0)\sin\phi + (z - z_0)\cos\phi \end{aligned} \tag{6}$$

Variables a and b are the equatorial radii (along the x and y axes) and c is the polar radius (along the z-axis for an ellipsoid with 0 deg inclination to the freestream). The angle ϕ is the angle between the major axis of the ellipsoid and the freestream flow. Coordinates (x_0, y_0, z_0) represent the centroid of the ellipsoid. Note that Q represents the total power deposited in the flow and $\iiint_{-\infty}^{\infty} S \mathrm{d}x\mathrm{d}y\mathrm{d}z = Q$.

III. Validation

LeMANS is validated for two different hypersonic cases. Simulations for hypersonic laminar airflow over blunt and sharp cones are compared to experimental work. These experimental validation cases are selected because they are considered representative of the two main types of realistic hypersonic air-vehicle geometries and because of the limited amount of experimental data available.

A. 3-D Sharp Elliptic Cone

3-D calculations are carried out for a Mach 8 sharp elliptic cone originally studied experimentally by Kimmel et al. [22,23]. The cone was mounted parallel to the freestream and consisted of a 2:1 aspect ratio, a half-angle along the major axis of 14 deg, and a length $L = 1.016$ m. It was machined from stainless steel with a 40 μm nose radius and surface roughness less than 0.81 μm. The flow conditions are listed in Table 1.

A structured grid is generated because it is known to produce better results than unstructured meshes in regions near the surface of the body and through a shock [24]. One quarter of the geometry is

Table 1 Flow conditions for the experiment of Kimmel et al. [22,23]

Parameter	Value
M	7.93
u_∞	1180.0 m/s
T_∞	54.6 K
T_w	303.0 K
T_0	728.0 K
p_∞	165.0 Pa
ρ_∞	0.011 kg/m^3
μ_∞	3.77×10^{-6} kg/m · s
Re_L	3.33×10^6

used in the simulation because planes of symmetry exist along the major and minor axes. The 40 μm nose radius is accounted for along the tip's minor axis, resulting in an 80 μm radius along the major axis because of the elliptic geometry.

The model is aligned with the x axis in the axial direction, the y axis in the horizontal direction, and the z axis in the vertical direction. A cylindrical coordinate system is also employed with $\theta = 0$ deg at the top centerline of the model (z axis) and $\theta = 90$ deg at the leading edge (y axis), as seen in Fig. 1.

A gradual increase in grid spacing is used along the conic body with the smallest spacing near the tip. Radial points are algebraically spaced to increase the number of points close to the body. Grid points are equally spaced along the circumference. As a result, cell clustering occurs near the surface and the tip of the body. A grid independence study is conducted with $i \times j \times k$ grid dimensions changing from $330 \times 40 \times 30$ to $440 \times 50 \times 40$ to $550 \times 60 \times 50$. Based on comparisons of the solutions obtained on these meshes the $440 \times 50 \times 40$ grid is considered sufficiently refined and is used in the rest of the analysis. See [25] for more details.

Cross-sectional slices of the computed surface conditions are extracted to match the locations of the experimental measurements. Figure 2a shows the nondimensional pressure along the circumference of the body at $x/L = 0.625$. The pressure is relatively constant from the top centerline ($\theta = 0$ deg) to the shoulder ($\theta = 45$ deg), followed by a noticeable rise between the shoulder and the leading edge ($\theta = 90$ deg). Kimmel et al. [22,23] also provided computational results from a parabolized Navier–Stokes (PNS) solver, which are included in the figures as an additional reference.

Although the cone is sharp, the formation of the boundary layer at its tip results in a noticeable rise in pressure and temperature near the stagnation point. This rise in pressure can be seen in Fig. 2b for two different rays. The pressure quickly relaxes as the flow proceeds along the rest of the cone due to the viscous interaction. It is worth noting that the PNS solution does not capture the behavior of the flowfield in the stagnation region of the cone because of the physical simplifications inherent in that method.

The high-length Reynolds number (Re_L) and overall length of the model cause the flow to transition to turbulence as it proceeds along the body. LeMANS does not currently have a turbulence model implemented, and so numerical results in the transitional and turbulent regions should be disregarded. Plots of the Stanton number as a function of Reynolds number are presented in Figs. 3a–3c for $\theta = 0$, 45, and 88 deg. In all three plots, the flow starts out laminar and then transitions to turbulent as it proceeds along the body. The measured data were for $Re_L = 1.7 \times 10^6$ and 6.6×10^6, whereas the case run by LeMANS has $Re_L = 3.3 \times 10^6$. Because of flow similarity, the length Reynolds number does not affect the Stanton number in the laminar region and LeMANS accurately predicts its distribution for these cases.

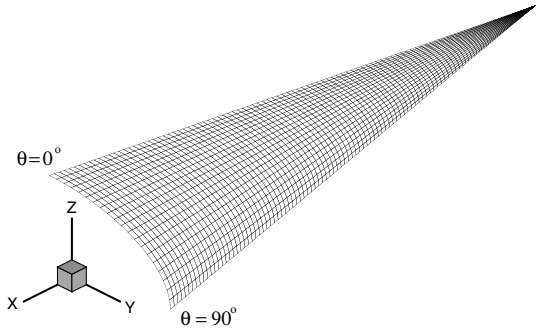

Fig. 1 Surface of the sharp elliptic cone grid with both Cartesian and cylindrical coordinate systems.

B. 3-D Blunt Elliptic Cone

A second 3-D validation study is performed on a Mach 14 blunt elliptic cone originally studied experimentally by Nowlan et al. [26] The model was mounted parallel to the freestream and had a 2:1 aspect ratio, a half-angle along the major axis of 10 deg, and a length $L = 0.21$ m. Details of cone geometry are provided in Fig. 4. The flow conditions are listed in Table 2.

A structured grid is generated following the same procedures and coordinate system as the sharp elliptic cone. A grid independence study is conducted with $i \times j \times k$ grid dimensions changing from $150 \times 30 \times 30$ to $300 \times 60 \times 60$ to $380 \times 80 \times 80$. The $300 \times 60 \times 60$ grid is considered sufficiently refined and is used in the rest of the analysis. Additional details on grid convergence are available in [25].

Figure 5 shows the nondimensional pressure along the circumference of the body at two axial locations and along two rays. Following a similar trend as the sharp cone observations, the pressure is relatively constant from the top centerline to the shoulder, followed by a gradual rise between the shoulder and the leading edge. The variation in pressure distribution along the rays is more dramatic compared with the sharp cone because the blunt-tip results in a strong detached bow shock and, consequently, a large stagnation region. Stanton number distributions in Fig. 6 show the profiles obtained with LeMANS follow the same general trends as those observed in the measurements.

Overpredictions observed in the nondimensional pressure and Stanton number distributions may be due to several influences not

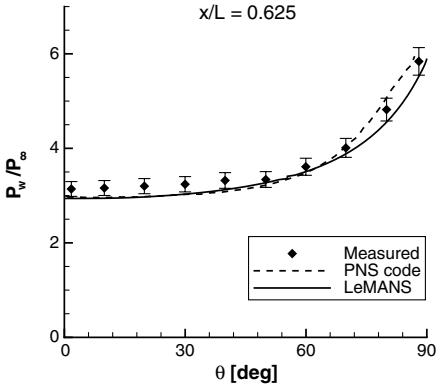

a) Pressure around the circumference

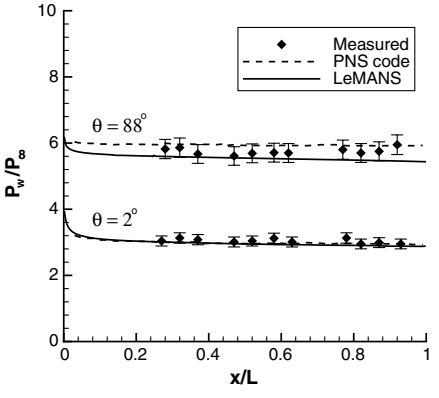

b) Pressure along rays

Fig. 2 Normalized surface pressure distributions for the Mach 8 sharp elliptic cone (±5% experimental uncertainty), with PNS calculations and experimental data from [22].

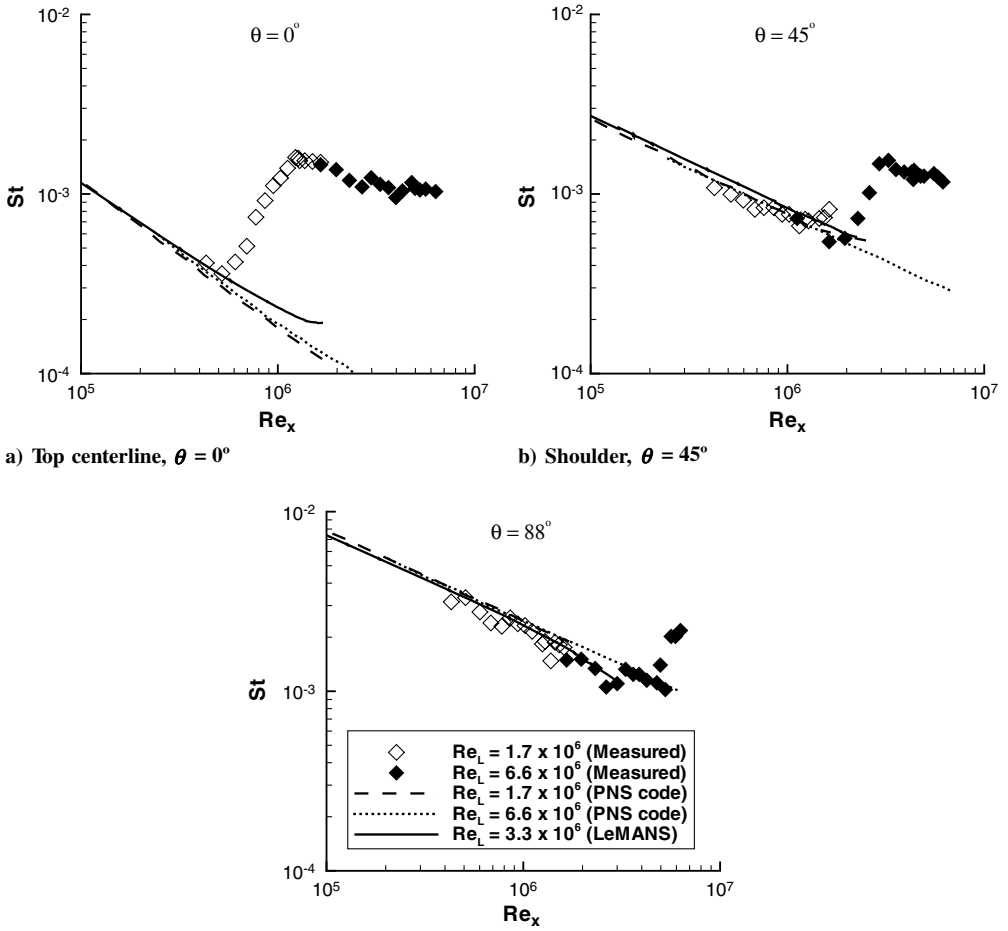

a) Top centerline, $\theta = 0^o$

b) Shoulder, $\theta = 45^o$

c) Leading edge, $\theta = 88^o$

Fig. 3 Stanton number distributions for the Mach 8 sharp elliptic cone (symbol size reflects ±10% experimental uncertainty), with experimental data and PNS calculations from [22].

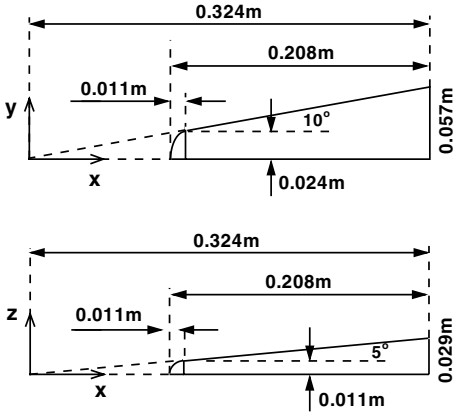

Fig. 4 Blunt elliptic cone geometry, from [26].

accounted for in the simulations. Nowlan et al. [26] noted an uncertainty of ±7 percent in the freestream flow conditions and the very cold freestream flow conditions ($T_\infty = 59.3$ K) could have lead to condensation on the nozzle. In addition, the CAL 48 in. shock tunnel could have developed "frozen" freestream conditions ($T_v \gg T_\infty$) as the flow accelerated through the nozzle. Nompelis et al. [27] computationally demonstrated that accounting for vibrational nonequilibrium freestream conditions greatly improved agreement between computational and experiment heat transfer measurements collected in a CAL shock tunnel for their hypersonic double-cone experiment. Despite the discrepancies, overall, LeMANS effectively demonstrates its capability of accurately computing 3-D hypersonic flows.

IV. Energy Deposition

The blunt elliptic cone geometry is selected to represent a fairly realistic hypersonic vehicle, with $L = 3$ m set as the representative vehicle length. Assuming the vehicle has constant material density, its center of gravity (CG) is located 1.95 m from the tip along the x axis ($x/L = 0.65$). The model is simulated in air at a 40 km altitude, a freestream velocity of 4000 m/s, and a 0 deg angle of attack. The complete flow conditions are provided in Table 3.

A grid independence study is conducted with $i \times j \times k$ grid dimensions changing from $300 \times 60 \times 60$ to $380 \times 80 \times 80$ to $400 \times 80 \times 120$. Grid independence is achieved with the $380 \times 80 \times 80$ grid that is used in the following simulations that include energy deposition. Details on the grid convergence study are available in [25].

Table 2 Flow conditions for run 15 of the Nowlan et al. experiment [26]

Parameter	Value
Mach	14.2
u_∞	2190. m/s
T_∞	59.3 K
T_w	294.0 K
T_0	211.0 K
p_∞	51.0 Pa
ρ_∞	0.003 kg/m^3
μ_∞	4.3×10^{-6} kg/m · s
Re_L	3.17×10^5

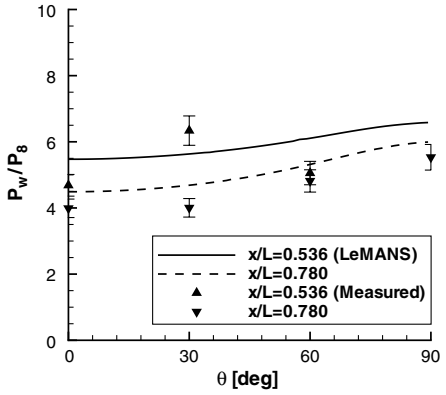

a) Pressure around the circumference

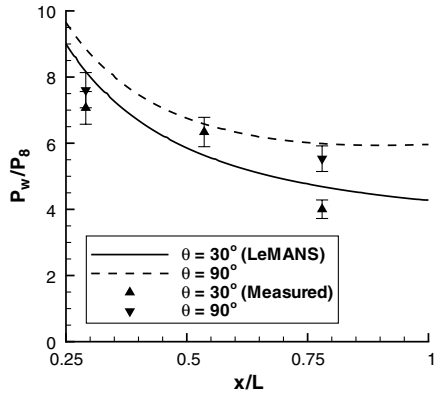

b) Pressure along rays

Fig. 5 Normalized surface pressure distributions for Mach 14 blunt elliptic cone (±7% experimental uncertainty), with experimental data from [26].

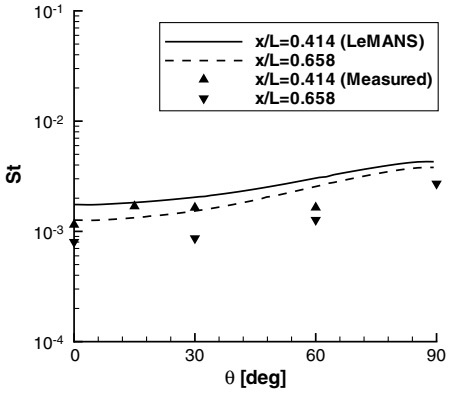

a) Stanton number around the circumference

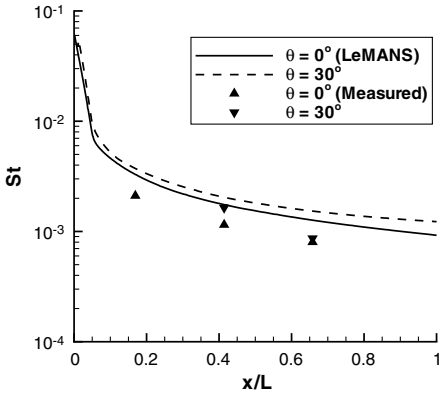

b) Stanton number along rays

Fig. 6 Stanton number distributions for Mach 14 blunt elliptic cone (symbol size reflects ±4.5% experimental uncertainty), with experimental data from [26].

A. Reference Pitching Moment

A nominal reference pitching moment is found by assuming a 2 deg flap with a cross-sectional area of 0.2×0.5 m is attached along the vehicle's top centerline as illustrated in Fig. 7. The size and location of the flap are based on illustrations of the hypersonic test vehicle shown in [28]. The control authority provided by the mechanical flap is estimated computationally by incorporating the flap with the blunt elliptic cone geometry.

The flap is accounted for in the blunt elliptic cone geometry by flaring the last 0.2 m of the cone. The flair extends around the circumference of the cone and has a 2 deg inclination. Extending the flair around the circumference of the body simplifies the geometry and eliminates unnecessary complexities (i.e., modeling the edge of the extended flap). Because the spanwise width of the actual flap extends 0.25 m ($\theta = 18$ deg) from the top centerline ($\theta = 0$ deg), the estimated control authority provided by the flap is computed by multiplying the increased body force within that region by its moment arm (1.05 m). This results in a pitching moment ($M_{p_{\text{flap}}}$) of 22.8 N · m.

Table 3 Flow conditions for Mach 12.6 airflow at an altitude of 40 km

Parameter	Value
Mach	12.6
u_∞	4000.0 m/s
T_∞	250.0 K
T_w	300.0 K
T_0	8300.0 K
p_∞	289.0 Pa
ρ_∞	0.004 kg/m^3
μ_∞	1.6×10^{-5} kg/m · s
Re_L	3.0×10^6

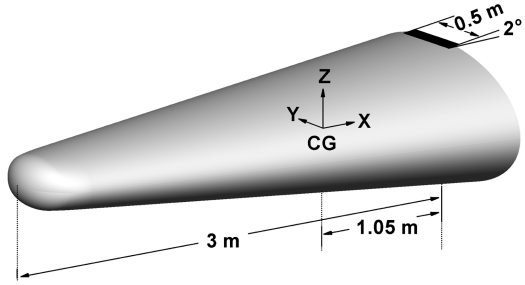

Fig. 7 Model of a 2 deg mechanical flap attached to a blunt elliptic body.

B. Parametric Study

To limit the scope of the problem, three volumetric deposition shapes are selected. Namely a sphere, pancake (oblate spheroid), and bean (prolate spheroid) are employed such that a representative volume of the ellipsoidal region ($V = 4/3\pi abc$) remains constant. The values used are listed in Table 4.

The centroid of the deposition is positioned along the top centerline ($y_0 = 0$ m) and is at least three characteristic length scales (λ) away from the surface of the body to ensure the entire deposition is deposited into the flowfield ($\iiint_{3\lambda}^{3\lambda} S\mathrm{d}x\mathrm{d}y\mathrm{d}z = 0.9999Q$). This distance is the minimum length from the centroid of a spherical deposition to the surface of the body as illustrated in Fig. 8:

$$x_0 = x_1 + 3\lambda \cdot \|n_{x_1}\| \tag{7}$$

$$z_0 = z_1 + 3\lambda \cdot \|n_{z_1}\| \tag{8}$$

Table 4 Deposition geometry parameters for a Mach 12 blunt elliptic cone ($L = 3$ m)

	a	b	c
Sphere	0.007 m	0.007 m	0.007 m
Pancake	0.01852 m	0.01852 m	0.001 m
Bean	0.001852 m	0.1 m	0.001852 m

$$\phi = \tan^{-1}\left\| \frac{n_{x_1}}{n_{z_1}} \right\| \tag{9}$$

With $3\lambda = 3a$, the values of z_0 and ϕ are determined for a given x_0 by enforcing Eqs. (7) and (8). This determines the location of $[x_1, z_1]$ and its outward unit normal vector **n**. Equation (9) is used to determine ϕ so that the polar radii of the ellipsoidal deposition aligns with **n**. The oblate spheroid is positioned so that its major axis is parallel to the freestream flow, whereas the major axis of the prolate spheroid is perpendicular to the freestream flow.

Using the Mach 5 flat plate experiment originally studied by Kimmel et al. [29,30] and recent magnetohydrodynamic power-generation experiments [31] for reference, realistic power input is assumed to lie in the range of 1 to 15 kW. The deposition is positioned near the nose of the vehicle tip to maximize the distance from the CG. This is done not only to increase the moment arm of the body force due to the deposition, but also because larger force changes are observed when the actuator is placed near the leading-edge bow shock [13]. The three deposition shapes are studied with variation of two additional parameters: the deposition input power (Q) and the distance along the body (x/L).

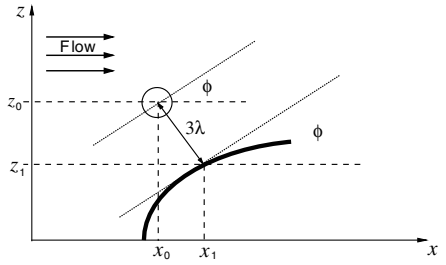

Fig. 8 The constant height parameter used to determine z_0 and ϕ.

The total amount of power deposited into the flow is characterized by the nondimensional total power deposition value $\tilde{Q}$:

$$\tilde{Q} = \frac{Q}{\rho_\infty u_\infty^3 L^2} \tag{10}$$

For the cases in the study $\tilde{Q} = 4.3 \times 10^{-7}$, 1.7×10^{-6}, and 6.5×10^{-6} for $Q = 1, 4$, and 15 kW, respectively. This parameter provides some information on vehicle and application scaling.

The axial location of the energy deposition is apparent after investigating the pressure coefficient and Stanton number along the top centerline ($\theta = 0$ deg) for the three shapes in Fig. 9. Although there is a slight increase in the Stanton number, it is accompanied by a noticeable rise in the pressure coefficient, particularly in the sphere and pancake depositions. This may be due to the fact that a sphere has the minimum surface area of a spheroid and, consequently, has the highest power deposited per projected surface area onto the body. The total force acting on the body is determined by numerical integration of the pressure and viscous force components over the body surface, using a method consistent with the finite-volume formulation of LeMANS.

With the local force known, the pitching moment is determined in the conventional manner. Because of the deposition on the top half of the vehicle, the pitching moment for each scenario is its deviation from the baseline ($M_p = M_{p_{\text{deposition}}} - M_{p_{\text{baseline}}}$). It is normalized by the moment due to the mechanical flap ($M_{p_{\text{flap}}} = 22.8$ N · m). Figure 10 plots the normalized change in pitching moment for each

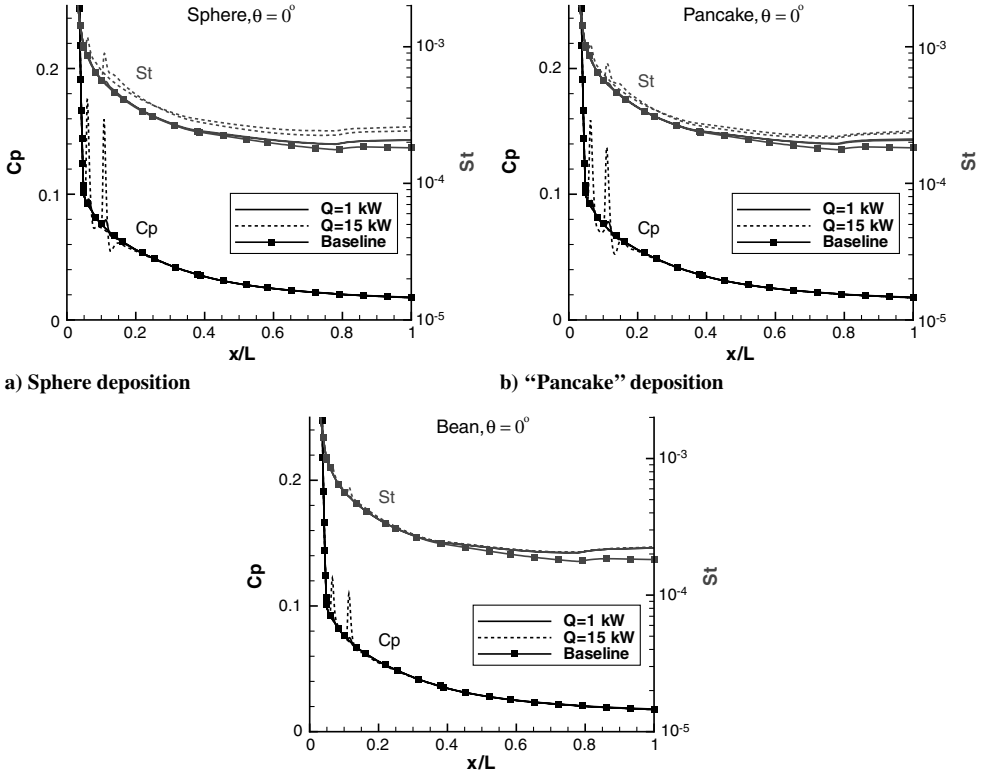

a) Sphere deposition

b) "Pancake" deposition

c) "Bean" deposition

Fig. 9 Pressure coefficient and Stanton number distributions for the Mach 12 blunt elliptic cone ($L = 3$ m) for various energy deposition patterns along the top centerline ($T_w = 300$ K).

of the shapes. The points are fitted with a parametric spline because of their assumed nonlinearity.

All simulations are computed assuming thermal equilibrium and use a 5-species finite-rate chemistry model (N_2, O_2, NO, N, and O) except for the largest deposition scenario ($Q = 50$ kW, $x/L = 0.10$, pancake). This scenario is repeated for two additional conditions: thermal equilibrium, 11-species chemistry model; and thermal nonequilibrium, 11-species chemistry model. The 11-species chemistry model (N_2, O_2, NO, N, O, N_2^+, O_2^+, NO^+, N^+, O^+, e) accounts for weakly ionized plasmas. These additional cases are compared against their respective baseline cases to determine the effectiveness of the deposition.

For thermal equilibrium air, the inclusion of a larger chemistry model has a relatively small impact on the total pitching moment as seen in the $Q = 50$ kW case [equilibrium, 5 sp (species) vs equilibrium, 11 sp]. Thermal nonequilibrium noticeably reduces the effectiveness of the energy deposition because only the energy going into the translational temperature can affect the local pressure and, thus, the net force. Comparing the results for the thermal equilibrium, 5-species simulations to the thermal nonequilibrium, 11-species simulations for the $Q = 30$, 50 kW cases, it is clear that thermal nonequilibrium and weakly ionized plasma effects become increasing significant as the total power deposited increases and the flow deviates from a perfect gas.

Figure 10 shows energy deposition is able to provide the same order of magnitude of control authority as the mechanical flap. In addition, although the shape of the deposition appears to have noticeable effects on the local pressure coefficient and Stanton number, it does not appear to have a large impact on the overall change in the pitching moment (control authority).

C. Hot Wall Effect

The previous simulations used a constant wall temperature of 300 K as seen Table 3. This is cooler than the expected wall temperature of a real hypersonic vehicle. Assuming blackbody emissivity ($\epsilon = 1$), the Stefan–Boltzmann Law is used along with the computed heat flux on the body to estimate the expected wall temperature:

$$T_w = \left(\frac{q_w}{\epsilon\sigma}\right)^{1/4} \tag{11}$$

This estimated wall temperature varies from 600–1900 K along the cone, with an average temperature of 1000 K in the region where the deposition would be located. A new set of simulations is carried out with $T_w = 1000$ K and all other conditions equal to those listed in Table 3. The simulations are performed using the pancake deposition parameters listed in Table 4 and the centroid of the deposition located at $x/L = 0.1$. The moment coefficient is calculated for each simulation using Eq. (12):

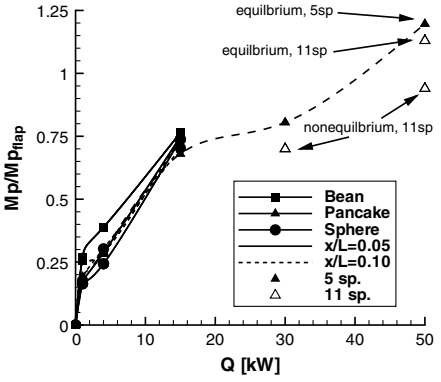

Fig. 10 Normalized change in pitching moment for a Mach 12 blunt elliptic cone ($L = 3$ m) for various energy deposition patterns ($T_w = 300$ K).

$$C_m = \frac{M_p}{\frac{1}{2}\rho_\infty u_\infty^2 L^2 d} \tag{12}$$

The reference area is taken to be the maximum spanwise width ($d = 1.644$ m) multiplied by the body length ($L = 3$ m). Figure 11 plots the moment coefficient vs power deposited for two constant wall temperatures. The higher wall temperature reduces the moment coefficient (control authority) of the vehicle because a larger portion of the energy deposited goes into the higher energy modes (i.e., rotation, vibration, and dissociation) instead of the translational energy mode.

V. Additional Vehicle Configurations

The freestream conditions used in the simulations of the 3 m configuration (Table 3) are also applied to two additional, scaled geometries. The "medium" scaled vehicle has a length $L = 0.62$ m. The nondimensional total power deposition value $\tilde{Q}$ for the cases run is $\tilde{Q} = 4.0 \times 10^{-5}$, 1.0×10^{-4}, and 1.5×10^{-4} for $Q = 4$, 10, and 15 kW, respectively.

The deposition is modeled as an oblate spheroid (pancake), scaled to match the one used in the $L = 3$ m parametric study. The energy deposition volume is positioned near the bow shock ($x/L = 0.10$) with its equatorial radii and polar radius set as $a = b = 0.00386$ m and $c = 0.00021$ m.

The moment coefficient for the simulations is found using Eq. (12) with $d = 0.343$ m. The pitching moment due to the mechanical flap is found following the approach covered in Sec. IV.A with the large geometry flap dimensions proportionately scaled (10.5×4.2 cm). This results in a pitching moment ($M_{p_{\text{flap}}}$) of 0.148 N · m. The smaller geometry produces a weaker bow shock and consequently a lower post-shock temperature. Similar to Sec. IV.C, the cooler temperature improves the control authority provided by energy deposition. However, a large spike in the Stanton number distribution is observed in Fig. 12. This coincides with the location of the deposition and partially recovers to the baseline distribution as the flow progresses along the body. The distribution can not fully recover because of the additional energy added to the flow.

The effects of energy deposition are also simulated for several cases using a "small" $L = 0.21$ m blunt elliptic cone with freestream conditions found in Table 2. These conditions represent an altitude of 42 km in air, based on the unit Reynolds number. The decrease in freestream velocity along with the significantly smaller geometry increases the nondimensional total power deposition value $\tilde{Q}$ by several orders of magnitude. For the cases' run, $\tilde{Q} = 4.0 \times 10^{-4}$, 8.0×10^{-4}, and 1.6×10^{-3} for $Q = 500$ W, 1 kW, and 2 kW, respectively.

The deposition is modeled as an oblate spheroid (pancake), similar to the one used in the $L = 3$ m parametric study. The energy deposition volume is positioned near the bow shock with its centroid at $x_0 = 0.0292$ m, $y_0 = 0$ m, and $z_0 = 0.017$ m, and its equatorial radii and polar radius are $a = 0.003$ m, $b = 0.004$ m, and $c =$ 0.001 m, with $\theta = 0$ deg. Unlike the medium cone, the deposition shape is larger than a proportionally scaled large cone deposition, and the deposition's polar radius is not quite aligned to the surface's normal vector (**n**). The parametric study presented in Sec. IV.B

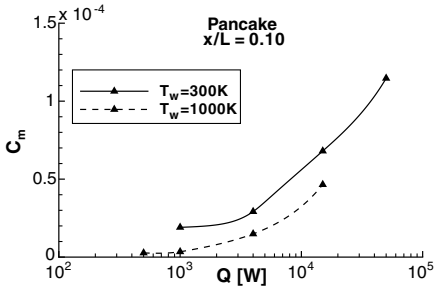

Fig. 11 Moment coefficient for a Mach 12 blunt elliptic cone ($L = 3$ m) for two constant wall temperatures.

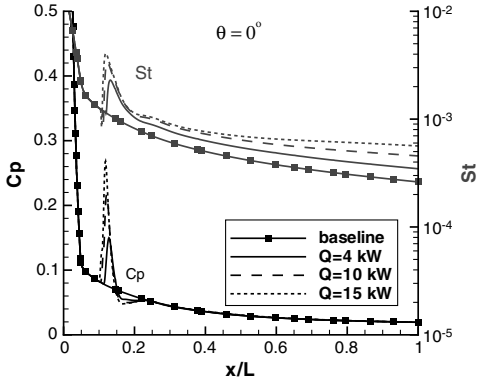

Fig. 12 Pressure coefficient and Stanton number distributions along the top center line ($\theta = 0$ deg) of a Mach 12 blunt elliptic cone ($L = 0.6$ m) with different amounts of energy deposition ($T_w = 300$ K).

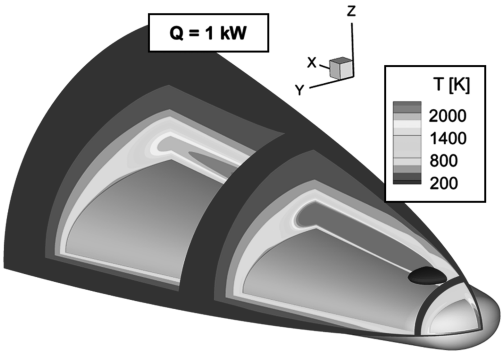

Fig. 13 Temperature contours for Mach 14 blunt elliptic cone (L= 0.2 m) with $Q = 1$ kW.

suggests the deposition shape has a minimal effect on the resulting pitching moment. This indicates these simulations are relevant and particularly useful when drawing conclusions across different configurations. The energy deposition is also positioned slightly farther from the nose than the previous case ($x/L = 0.14$).

Compared with the previous configurations, the small geometry produces an even weaker bow shock, which further reduces the post-shock temperature. In addition, the freestream temperature and total enthalpy are much lower in these simulations (refer to Table 2). This allows for a larger portion of the deposition to increase the translational temperature (net force increase). In addition, the shorter body length (L) means the flow passes over the vehicle quicker, and so the large temperature rise observed within the region of the deposition extends farther along the vehicle. This is apparent in the significant downstream temperatures observed in Fig. 13, where the deposition is illustrated as the oblate spheroid centered above the top centerline near the leading bow shock.

Coinciding with the high temperature, a strong heat transfer penalty is detected, along with a dramatic increase in the pressure coefficient distribution (Fig. 14). Although the Stanton number remains significantly elevated downstream of the deposition, the pressure coefficient quickly returns to the baseline (equilibrium) state, which is consistent to the observations seen in the large and medium cone simulations.

The moment coefficient is found using Eq. (12) with d= 0.114 m. Consistent with previous simulations, the pitching moment due to the mechanical flap is computed following the method presented in Sec. IV.A with the large geometry flap dimensions scaled down proportionately (3.5×1.4 cm). This results in a pitching moment ($M_{p_{\text{flap}}}$) of 10^{-3} N · m.

These results, along with those obtained for the medium and large blunt elliptic cone simulations, are plotted together in Fig. 15 using the nondimensional total power deposition parameter $\tilde{Q}$. Figure 15a shows a strong correlation between $\tilde{Q}$ and the moment coefficient for the various simulations. As previously noted, the scale deposition shape of the small cone does not exactly match the medium or large

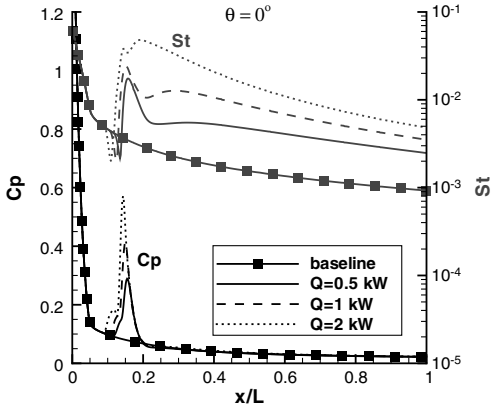

Fig. 14 Pressure coefficient and Stanton number distributions along the top center line ($\theta = 0$ deg) of a Mach 14 blunt elliptic cone ($L = 0.2$ m) with various levels of energy deposition ($T_w = 294$ K).

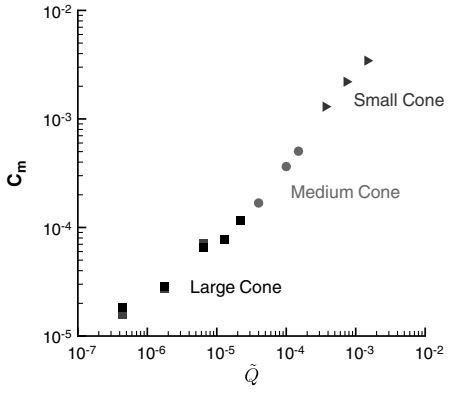

a) Moment coeffcient

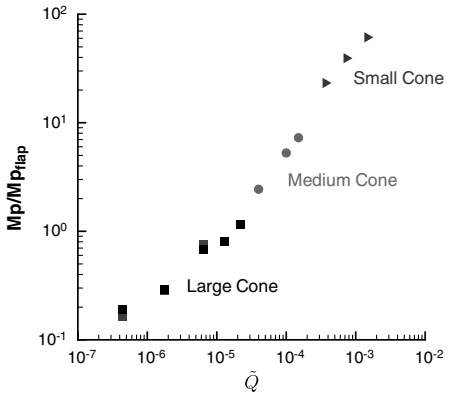

b) Nondimensional pitching moment

Fig. 15 Moment coefficient and normalized change in pitching moment vs the nondimensional total power deposition $\tilde{Q}$ for various vehicle configurations ($T_w = 300$ K, thermal equilibrium, 5 sp, pancake deposition).

cones, but these results further demonstrate the minimal contribution deposition shape has on the net control authority. The results appear to follow a near linear curve when plotted on a log–log scale ($C_m \approx \tilde{Q}^{1.1}$). The different deposition locations, along with different vehicle lengths and freestream conditions, and real gas effects cause the results to deviate slightly from the linear curve.

Using the reference pitching moment found for each of the configurations, the normalized pitching moment for each configuration is plotted in Fig. 15b. Again, the results follow a near-linear curve on a log–log scale ($M_p/M_{p\text{flap}} \approx \tilde{Q}^{1.3}$) with deviations from the curve due to the aforementioned reasons. The figure shows that energy deposition is a viable replacement for a mechanical flap when $\tilde{Q} \geq 10^{-5}$. Given that $\tilde{Q} = Q/\rho_\infty u_\infty^3 L^2$, this suggests smaller geometries, flying at lower velocities and/or higher altitudes (lower

densities) would make energy deposition a viable replacement for a mechanical flap. A full table of the pitching moment (M_p) for all simulations is available in [32].

VI. Conclusions

A numerical study was performed to investigate whether a practical level of control could be achieved from volumetric energy deposition for a realistic hypersonic vehicle. Using a phenomenological heating model, a parametric study was completed investigating the shape, location, and total amount of energy volumetrically deposited into the flowfield for a blunt-nosed elliptic cone configuration. The shape of the deposition resulted in relatively small changes in the effectiveness of the deposition, whereas an increased wall temperature noticeably decreased the moment coefficient. Thermal nonequilibrium and weakly ionized plasma effects also decrease the control authority as input power increases. The effectiveness of volumetric energy deposition for flight control appeared to scale strongly with the nondimensional parameter based on the freestream flow kinetic energy flux. It appears to be a viable means of control for configurations at higher altitude, with slower velocities and smaller vehicle length.

There is an ongoing effort to replace the phenomenological energy deposition model with a magnetohydrodynamic model in low magnetic Reynolds number approximation. This should provide useful insight by providing a more physical representation of the energy deposition physics.

Acknowledgments

The authors are indebted to the Michigan/AFRL/Boeing Collaborative Center in Aeronautical Sciences, which provided funding to the first author. The first author would like to thank Leonardo Scalabrin for numerous discussions about LeMANS and Roger Kimmel for his valuable discussions on the subject. The generous use of the University of Michigan's Center for Advanced Computing and the Aeronautical Systems Center Major Shared Resource Center (ASC MSRC) were indispensable to this investigation and are greatly appreciated.

References

[1] Fomin, V. M., Tretyakov, P. K., and Taran, J.-P., "Flow Control Using Various Plasma and Aerodynamic Approaches," *Aerospace Science and Technology*, Vol. 8, No. 5, 2004, pp. 411–421. doi:10.1016/j.ast.2004.01.005

[2] Shang, J. S., Surzhikov, S. T., Kimmel, R., Gaitonde, D., Menart, J., and Hayes, J., "Mechanisms of Plasma Actuators for Hypersonic Flow Control," *Progress in Aerospace Sciences*, Vol. 41, No. 8, 2005, pp. 642–668. doi:10.1016/j.paerosci.2005.11.001

[3] Mason, W. H., and Lee, J., "Aerodynamically Blunt and Sharp Bodies," *Journal of Spacecraft and Rockets*, Vol. 31, No. 3, 1994, pp. 378–382. doi:10.2514/3.26449

[4] Santos, W. F. N., and Lewis, M. J., "Aerothermodynamic Performance Analysis of Hypersonic Flow on Power Law Leading Edges," *Journal of Spacecraft and Rockets*, Vol. 42, No. 4, 2005, pp. 588–597. doi:10.2514/1.9550

[5] Shang, J. S., Hayes, J., and Menart, J., "Hypersonic Flow over a Blunt Body with Plasma Injection," *Journal of Spacecraft and Rockets*, Vol. 39, No. 3, 2002, pp. 367–375. doi:10.2514/2.3835

[6] Kremeyer, K., Sebastian, K., and Shu, C.-W., "Computational Study of Shock Mitigation and Drag Reduction by Pulsed Energy Lines," *AIAA Journal*, Vol. 44, No. 8, 2006, pp. 1720–1731. doi:10.2514/1.17854

[7] Yan, H., and Gaitonde, D., "Control of Edney IV Interaction by Energy Pulse," AIAA Paper 06-562, Jan. 2006.

[8] Riggins, D. W., and Nelson, H. F., "Hypersonic Flow Control Using Upstream Focused Energy Deposition," *AIAA Journal*, Vol. 38, No. 4, 2000, pp. 723–725. doi:10.2514/2.1020

[9] Macheret, S. O., Shneider, M. N., and Miles, R. B., "Magnetohydrodynamic Control of Hypersonic Flows and Scramjet Inlets Using Electron Beam Ionization," *AIAA Journal*, Vol. 40, No. 1, 2002, pp. 74–81. doi:10.2514/2.1616

[10] Shang, J. S., Kimmel, R. L., Menart, J., and Surzhikov, S. T., "Hypersonic Flow Control Using Surface Plasma Actuator," *Journal of Propulsion and Power*, Vol. 24, No. 5, 2008, pp. 923–934. doi:10.2514/1.24413

[11] Girgis, I. G., Shneider, M. N., Macheret, S. O., Brown, G. L., and Miles, R. B., "Creation of Steering Moments in Supersonic Flow by Off-Axis Plasma Heat Addition," AIAA Paper 02-129, Jan. 2002.

[12] Gnemmi, P., Charon, R., Dupéroux, J.-P., and George, A., "Feasibility Study for Steering a Supersonic Projectile by a Plasma Actuator," *AIAA Journal*, Vol. 46, No. 6, 2008, pp. 1308–1317. doi:10.2514/1.24696

[13] Menart, J., Stanfield, S., Shang, J., Kimmel, R., and Hayes, J., "Study of Plasma Electrode Arrangements for Optimum Lift in a Mach 5 Flow," AIAA Paper 06-1172, Jan. 2006.

[14] Updike, G. A., Shang, J. S., and Gaitonde, D. V., "Hypersonic Separated Flow Control Using Magneto-Aerodynamic Interaction," AIAA Paper 05-164, Jan. 2005.

[15] Kimmel, R. L., Hayes, J. R., Crafton., J. W., Fonov, S. D., Menart, J., and Shang, J., "Surface Discharge for High-Speed Boundary Layer Control," AIAA Paper 06-710, Jan. 2006.

[16] Miles, R. B., Macheret, S. O., Shneider, M. N., Steeves, C., Murray, R. C., Smith, T., and Zaidi, S. H., "Plasma-Enhanced Hypersonic Performance Enabled by MHD Power Extraction," AIAA Paper 05-561, Jan. 2005.

[17] Scalabrin, L. C., and Boyd, I. D., "Development of an Unstructured Navier–Stokes Solver For Hypersonic Nonequilibrium Aerothermodynamics," AIAA Paper 05-5203, June 2005.

[18] Scalabrin, L. C., and Boyd, I. D., "Numerical Simulation of Weakly Ionized Hypersonic Flow for Reentry Configurations," AIAA Paper 06-3773, June 2006.

[19] Scalabrin, L. C., and Boyd, I. D., "Numerical Simulation of the FIRE-II Convective and Radiative Heating Rates," AIAA Paper 07-4044, June 2007.

[20] Scalabrin, L. C., "Numerical Simulation of Weakly Ionized Hypersonic Flow Over Reentry Capsules," Ph.D. Dissertation, Univ. of Michigan, 2007.

[21] Poggie, J., "Plasma-Based Hypersonic Flow Control," AIAA Paper 06-3567, June 2006.

[22] Kimmel, R. L., Poggie, J., and Schwoerke, S. N., "Laminar-Turbulent Transition in a Mach 8 Elliptic Cone Flow," *AIAA Journal*, Vol. 37, No. 9, 1999, pp. 1080–1087. doi:10.2514/2.836

[23] Kimmel, R., Klein, M., and Schwoerke, S., "Three-Dimensional Hypersonic Laminar Boundary-Layer Computations for Transition Experiment Design," *AIAA Journal*, Vol. 34, No. 4, 1997, pp. 409–415.

[24] Candler, G., "Unstructured Grid Approaches for Accurate Aeroheating Simulations," AIAA Paper 07-3959, June 2007.

[25] Bisek, N. J., Boyd, I. D., and Poggie, J., "Numerical Study of Energy Deposition Requirements for Aerodynamic Control of Hypersonic Vehicles," AIAA Paper 08-1109, Jan. 2008.

[26] Nowlan, D., Burke, A., and Bird, K., "Pressure and Heat Transfer Distribution on ASD Elliptic Cone (W3) and ASD Sortie (W4) in the CAL 48-Inch Hypersonic Shock Tunnel," Cornell Aeronautical Laboratory, Inc., Rept. AM-1800-Y-2, Buffalo, NY, Dec. 1963, ASC 94 2649.

[27] Nompelis, I., Candler, G., and Holden, M., "Effect of Vibrational Nonequilibrium on Hypersonic Double-Cone Experiments," *AIAA Journal*, Vol. 41, No. 11, 2003, pp. 2162–2169. doi:10.2514/2.6834

[28] Walker, S. H., and Rodgers, F., "Falcon Hypersonic Technology Overview," AIAA Paper 05-3253, May 2005.

[29] Kimmel, R. L., Hayes, J. R., Menart, J. A., and Shang, J., "Effect of Surface Plasma Discharges on Boundary Layers at Mach 5," AIAA Paper 04-509, Jan. 2004.

[30] Kimmel, R., Hayes, J., Menart, J., and Shang, J., "Supersonic Plasma Flow Control Experiments," U.S. Air Force Research Laboratory, Rept ARFL-VA-WP-TR-2006-3006, Wright–Patterson AFB, OH, Dec. 2005, AFRL/WS 06-0097.

[31] Velocci, A. L. J., "A General Atomics-Led Team," *Aviation Week and Space Technology*, March 2007, p. 36.

[32] Bisek, N. J., Boyd, I. D., and Poggie, J., "Numerical Study of Plasma-Assisted Aerodynamic Control for Hypersonic Vehicles," AIAA Paper 08-4226, June 2008.

A. Ketsdever
Associate Editor